processes

MDPI

Article

Impact of Deep Shale Gas Dense-Cutting Fracturing Parameters on EUR

Tianyi Wang [1,2,3], Guofa Ji [1,2,3,*], Jiansheng Liu [4] and Zelong Xie [2,5]

[1] Cooperative Innovation Center of Unconventional Oil and Gas, Ministry of Education & Hubei Province, Yangtze University, Wuhan 430100, China; 2022710280@yangtzeu.edu.cn
[2] Hubei Key Laboratory of Oil and Gas Drilling and Production Engineering, Yangtze University, Wuhan 430100, China; 2022710273@yangtzeu.edu.cn
[3] State Key Laboratory of Low Carbon Catalysis and Carbon Cioxide Utilization, Yangtze University, Wuhan 430100, China
[4] Oil and Gas Technology Research Institute, Petro China Changqing Oilfield Company, Xi'an 710000, China; ljs62_cq@petrochina.com.cn
[5] National Engineering Research Center for Oil & Gas Drilling and Completion Technology, School of Petroleum Engineering, Yangtze University, Wuhan 430100, China
* Correspondence: jiguofa@163.com

Abstract: Deep shale formations pose significant challenges in forming high-conductivity fractures, leading to low ultimate recoverable reserves (EUR) per well under conventional fracturing techniques. Dense-cutting fracturing is a commonly employed method to enhance the EUR of individual wells; however, the critical process parameters influencing EUR remain unclear. This study develops a novel EUR calculation model tailored for deep shale gas dense-cutting, integrating the Warren-Root model with the constant-volume gas reservoir material balance equation. The model comprehensively incorporates Knudsen diffusion and adsorption-desorption phenomena in deep shale gas, corrects apparent permeability, and employs the finite element method to simulate dynamic pressure depletion during production. The study examines the impact of fracture half-lengths, cluster spacing, fracture conductivity and horizontal section lengths on EUR under tight-cutting fracturing. Orthogonal experiments combined with multiple linear regression analysis reveal the hierarchy of influence among the four factors on EUR: horizontal section length > fracture half-length > cluster spacing > fracture conductivity. The study derives EUR correlation expressions that incorporate the effects of crack half-length, cluster spacing, fracture conductivity, and horizontal segment length. The orthogonal experimental results indicate that EUR exhibits positive correlations with crack half-length, fracture conductivity, and horizontal segment length, while showing a negative correlation with cluster spacing. The multiple regression equation achieves a coefficient of determination (R^2) of 0.962 and an average relative error of 3.79%, outperforming traditional prediction methods in both accuracy and computational simplicity. The findings are of substantial significance for the rapid estimation of EUR in individual wells following deep shale gas fracturing and offer valuable theoretical insights for practical engineering applications.

Keywords: deep shale gas; dense-cutting fracturing parameters; EUR; multiple regression

check for updates

Academic Editors: Federica Raganati and Vijaya Raghavan

Received: 26 November 2024
Revised: 26 December 2024
Accepted: 30 December 2024
Published: 31 December 2024

Citation: Wang, T.; Ji, G.; Liu, J.; Xie, Z. Impact of Deep Shale Gas Dense-Cutting Fracturing Parameters on EUR. *Processes* **2025**, *13*, 66. https://doi.org/10.3390/pr13010066

Copyright: © 2024 by the authors. Licensee MDPI, Basel, Switzerland. This article is an open access article distributed under the terms and conditions of the Creative Commons Attribution (CC BY) license (https://creativecommons.org/licenses/by/4.0/).

1. Introduction

The development of shale gas internationally has progressively transitioned from shallow to deep layers. In the United States, the significance of deep shale gas development within the natural gas production and development landscape has steadily risen [1]. Since

the groundbreaking advancement of horizontal well segmented fracturing technology in 2007, the approach has evolved from fewer segments and clusters to the use of multiple segments and clusters, significantly enhancing efficiency and productivity [2]. China also possesses rich deep shale gas resources. Literature research [3–7] indicates that the recoverable resources of shale gas at depths ranging from 3000 m to 6000 m are approximately 20.93×10^{12} m^3, with an average gas content ranging from 4.0 t/m^3 to 6.5 t/m^3. Deep shale is characterized by high overburden pressure and elevated ambient temperature, with the in-situ stress coefficient approximately 2.0. The formation ambient temperature exceeds 120 °C, and the closure pressure surpasses 90 MPa. Consequently, it is challenging to form a complex fracture network and difficult to generate a high-conductivity fracture under conventional fracturing [8,9], resulting in a low Estimated Ultimate Recovery (EUR) for individual wells. Addressing how to enhance the EUR of individual wells and achieve efficient development is currently an urgent issue requiring attention.

Recently, In the process of research on the development of shale gas in the middle and shallow layers, it has been found that shortening the cluster spacing has a promoting effect on increasing production [10–13]. This observation has prompted the introduction of dense-cutting fracturing modification technology. The dense -cutting fracturing techniques enhance fracture complexity by reducing the spacing between clusters, thereby improving the utilization of reserves in previously under-stimulated zones to achieve higher Estimated Ultimate Recovery (EUR). Many scholars have begun to apply dense-cutting fracturing to the development of deep shale and study the effect of fracturing parameters on production. Cheng [14] developed a reservoir simulation model to explore the influence of the number of injection clusters and cluster spacing on production. The study suggested that reducing cluster spacing can notably boost shale gas reservoir production. Cote [15] and fellow researchers illustrated the feasibility of enhancing EUR by augmenting fracture strength through the reduction of cluster spacing. They also proposed that, under fixed conditions, increasing EUR is achievable by expanding the spacing between clusters, which is attainable through elevated fracture strength. Kristyn [16] and colleagues explored the impact of fracture shape and cluster spacing on production. They concluded that optimizing the spacing between clusters and fracture geometry is a pivotal factor in enhancing the EUR of a single well. Zheng [17] and co-researchers identified the implementation of the "intensive stage + high-strength proppant" method in the field. They determined that applying the "intensive stage + high-strength proppant" method in the field can augment the reservoir's production enhancement effect by reducing the spacing between clusters and enhancing the flow-conducting ability of fractures. Li et al. [18] summarized the hydraulic fracturing methods for shale oil fields in China, showing that the current development of shale oil has shifted to 6–12 clusters per segment, using high-density cutting to increase strength, reduce costs, and achieve increased production. Yang et al. [19] applied dense -cutting fracturing technology to deep coal and rock formations, achieving peak gas production of 6.0×10^4 m^3/d and achieving efficient development of deep coal and rock gas. Guo et al. [20] and Hu et al. [21] found in their study of tight sandstone that increasing the density of hydraulic fractures achieved effective utilization of sandstone reservoirs, with higher single -well recovery rates (EUR). The process parameters impacting the EUR of deep shale gas under intensive stage fracturing include cluster spacing, fracture half-length, horizontal section length, fracture conductivity, etc. [22–24]. However, the key process parameters affecting the EUR of deep shale gas and the correlation between these parameters and EUR have not been studied.

Traditional methods for estimating EUR typically encompass empirical approaches, contemporary declining production analysis, simulation prediction methods, probabilistic techniques, and empirical production decline curve analyses [25–29]. Due to the charac-

teristics of the seepage mechanism in deep shale gas reservoirs, it is difficult to accurately calculate the EUR of deep shale gas using the above methods [30].

In response to these challenges, this study develops a comprehensive deep shale gas tight-cutting EUR computation model. It is grounded in the Warren-Root model and the material balance equation tailored for fixed-capacity gas reservoirs. Additionally, dynamic pressure depletion during deep shale gas production is simulated through the finite element method. The study extensively investigates the impacts of engineering factors, including fracture half-lengths, cluster spacing, fracture conductivity, and horizontal section lengths, on the Estimated Ultimate Recovery (EUR) under dense-cutting fracturing of deep shale gas. Furthermore, the study employs orthogonal analysis and multivariate linear regression to scrutinize the correlations between these factors and EUR. The ultimate goal is to establish a correlation equation for EUR, enabling rapid prediction of EUR in deep shale gas and providing theoretical guidance for practical engineering applications.

2. Methodology

2.1. Deep Shale Gas EUR Calculation Model

Deep shale can be conceptualized as a gas reservoir with a fixed volume, and the pressure drop equation for such a closed gas reservoir can be derived from the material balance equation [31], as shown below:

$$\frac{p}{z} = \frac{p_i}{z_i}\left(1 - \frac{G_p}{G}\right) \tag{1}$$

where: p_i is the original formation pressure, MPa; G is the controlled gas reserves, m^3; z is the compression factor of gas; p is the current reservoir average pressure, MPa; z_i is the compression factor at the original formation pressure; and G_p is the cumulative gas production, m^3.

The governing equation for shale gas reservoirs is as follows:

$$G = A_g h \rho_s \delta \tag{2}$$

where: A_g is the gas-bearing area, km^2; δ is the gas content measured, t/m^3; h is the reservoir thickness, m; ρ_s is shale density, kg/m^3.

Utilizing the DAK (Dranchuk-Abu-Kassem) method [32], the deviation factor z can be determined, as follows:

$$\begin{aligned} z = {} & 1 + [A_1 + \tfrac{A_2}{T_{Pr}} + \tfrac{A_3}{T_{Pr}^3} + \tfrac{A_4}{T_{Pr}^4} + \tfrac{A_5}{T_{Pr}^5}]\rho_{Pr} \\ & + [A_6 + \tfrac{A_7}{T_{Pr}} + \tfrac{A_8}{T_{Pr}^2}]\rho_{Pr}^2 - A_9[\tfrac{A_7}{T_{Pr}} + \tfrac{A_8}{T_{Pr}^2}]\rho_{Pr}^5 \\ & + A_{10}(1 + A_{11}\rho_{Pr}^2)\tfrac{\rho_{Pr}^2}{T_{Pr}^3}\exp(1 - A_{11}\rho_{Pr}^2) \end{aligned} \tag{3}$$

where: the values of A_1 to A_{11} are as follows: $A_1 = 0.3265$, $A_2 = -1.0700$, $A_3 = -0.5339$, $A_4 = 0.01569$, $A_5 = -0.05165$, $A_6 = 0.5475$, $A_7 = -0.7361$, $A_8 = 0.1844$, $A_9 = 0.1056$, $A_{10} = 0.6134$, $A_{11} = 0.7210$; ρ_{Pr} is the contrast density, kg/m^3; T_{Pr} is the proposed comparison temperature, K.

2.2. Matrix-Fracture Permeability Modeling of Deep Shale

The variation in the mean reservoir pressure (p) during production is simulated using matrix-fracture permeability modeling of deep shale employing the following physical model (Figure 1).

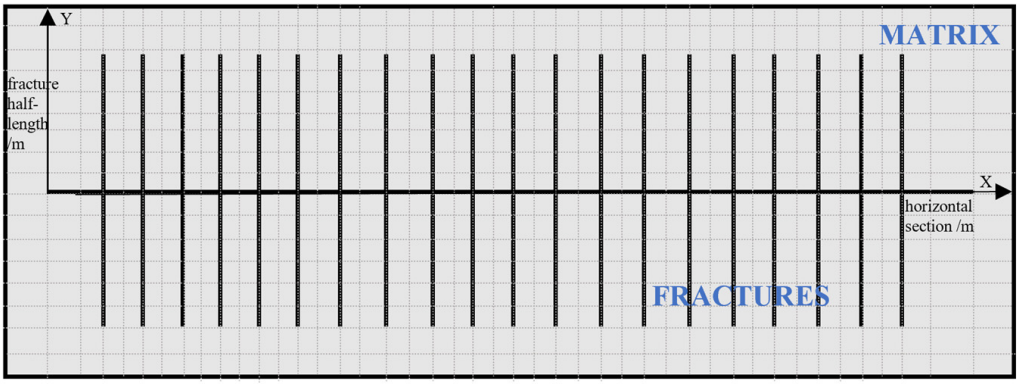

Figure 1. The physical model of intensive stage fracturing in Shale Horizontal Wells.

Owing to the elevated temperature and high-pressure physical characteristics of deep shale, the desorption phenomenon of shale gas becomes more pronounced, affecting both permeability and seepage. Therefore, the isothermal adsorption equation is incorporated into the model to depict desorption and adsorption in the matrix. The Warren-Root model [33] serves as the mathematical foundation for the matrix-fracture seepage model, as shown below.

1. Matrix Permeability Model

$$\frac{\partial}{\partial x}\left(\frac{\rho_g K_{app}}{\mu_g}\frac{\partial p_m}{\partial x}\right)+\frac{\partial}{\partial y}\left(\frac{\rho_g K_{app}}{\mu_g}\frac{\partial p_m}{\partial y}\right)-\frac{\rho_g K_{app}\alpha\left(p_m-p_f\right)}{\mu_g}=\frac{\partial}{\partial t}\left(\phi_m\rho_g+(1-\phi_m)\frac{\rho_s M_g}{V_{std}}\frac{V_L p_m}{p_L+p_m}\right) \tag{4}$$

$$\alpha=8\left(\frac{1}{L_x^2}+\frac{1}{L_y^2}+\frac{2}{L_x L_y}\right) \tag{5}$$

$$\rho_g=\frac{p_{\mathrm{m}} Mmol}{RT} \tag{6}$$

$$\mu_g=10^{-4}\frac{(22.650+0.0388M_g)T^{1.5}}{(209.2+19.26M_g+1.8T)}\exp\left(X\left(\frac{0.12037p_m M_g}{zT}\right)^{Y}\right) \tag{7}$$

where: ρ_g is the gas density, kg/m^3; μ_g is the gas viscosity, Pa·s; K_{app} is the apparent permeability, mD; ϕ_m is the matrix porosity, dimensionless; p_m is the matrix pressure, MPa; p_f is the fracture pressure, MPa; V_L is the Langmuir volume, m^3/kg; p_L is the Langmuir pressure, MPa; ρ_s is the shale density, kg/m^3; M_g is the gas molecular mass, kg/mol; V_{std} is the molar volume of gas at standard conditions, m^3/mol; α is the shape factor, m^{-1}; L_x, L_y are the length of the matrix in x, y direction, m; T is the formation temperature, K; R is the gas universal constant, R = 0.008314 MPa·m^3/(mol·K); $Mmol$ is the gas molar mass, kg/mol; X and Y are coefficients, X = 551.448 + 0.01 Mg; Y = 2.447−0.224X.

Deep shale gas exhibits low porosity. To characterize the microscopic flow of shale gas within the pores, Guo [34] and Yang [35], among others, considered the Knudsen diffusion phenomenon and gas desorption in the pores, leading to the derivation of an apparent permeability model, as shown below:

$$K_{app}=\frac{r_e^4}{r_0^4}\left[1+\frac{128}{15\pi^2}\arctan\left(4Kn_e^{0.4}\right)Kn_e\right]\left(1+\frac{4Kn_e}{1+Kn_e}\right)k_\infty \tag{8}$$

$$Kn_e=\frac{K_B T}{\sqrt{2}\pi\delta_i^2 p r_e}\times 10^{-6} \tag{9}$$

$$r_e=r_0-d_{CH_4}\frac{p_{\mathrm{m}}}{p_L+p_m} \tag{10}$$

where: Kn_e is the Knudsen number considering adsorption; r_e is the pore radius considering adsorption; K_B is the Boltzmann's constant, with a value of 1.3805×10^{-23} J·K^{-1}; δ_i is the effective collision diameter of methane gas molecules, with a value of 0.4×10^{-9} m; p is the gas pressure, MPa; r_0 is the initial pore radius, m; d_{CH4} is the molecular diameter of methane.

2. Fracture Permeability Model

Fracturing deep shale reservoirs establishes a flow pathway from horizontal fractures to the wellbore. The flow of gas molecules in this space can be treated in accordance with Darcy's law, expressed as [36]:

$$\frac{\partial}{\partial_x}\left(\frac{\rho_g K_f}{\mu_g}\frac{\partial_{P_f}}{\partial_x}\right)+\frac{\partial}{\partial_y}\left(\frac{\rho_g K_f}{\mu_g}\frac{\partial_{P_f}}{\partial_y}\right)+\frac{\rho_g K_{app}\alpha\left(p_m-p_f\right)}{\mu_g}-q_{well}=\frac{\partial\left(\phi_f\rho_g\right)}{\partial_t} \tag{11}$$

where: ϕ_f is the fracture porosity, dimensionless, K_f is the fracture permeability, mD, q_{well} is the scuttle flow from fractures to the horizontal wellbore, m^3/d.

The deep shale is considered a confined reservoir. The pressure at the outer boundary is assumed to be zero, while the inner boundary pressure is equated to the wellbore pressure, providing boundary conditions for the analysis. The internal and external boundary conditions are imposed on the matrix below:

$$\begin{cases} \frac{\partial_{pm}}{\partial_x}\Big|_{x=0}=0,\ \frac{\partial_{pm}}{\partial_x}\Big|_{x-X_e}=0 & \text{(outer boundary conditions)} \\ \frac{\partial_{pm}}{\partial_y}\Big|_{y=0}=0,\ \frac{\partial_{pm}}{\partial_y}\Big|_{y-Y_e}=0 & \text{(outer boundary conditions)} \\ p_m\Big|_{(x=0,y=0)}=p_{wf} & \text{(internal boundary conditions)} \end{cases} \tag{12}$$

where: Y_e and X_e are the boundaries perpendicular and parallel to the fracture direction in shale gas reservoirs, respectively, measured in meters; p_{wf} is the bottom pressure in shale gas wells, measured in Pascals.

The internal and external boundary conditions of the fracture system are the following:

$$\begin{cases} \frac{\partial p_f}{\partial_x}\Big|_{x=L_f}=0,\ \frac{\partial p_f}{\partial_y}\Big|_{y=L_f}=0 & \text{(outer boundatry conditions)} \\ p_f\Big|_{(x=0,y=0)=p_{wf}} & \text{(internal boundary conditions)} \end{cases} \tag{13}$$

The initial conditions are as follows:

$$\begin{cases} p_{\mathrm{m}}|_{t=0}=p_i \\ p_f\Big|_{t=0}=p_i \end{cases} \tag{14}$$

The flow chart of the methodology used in this study is shown in Figure 2.

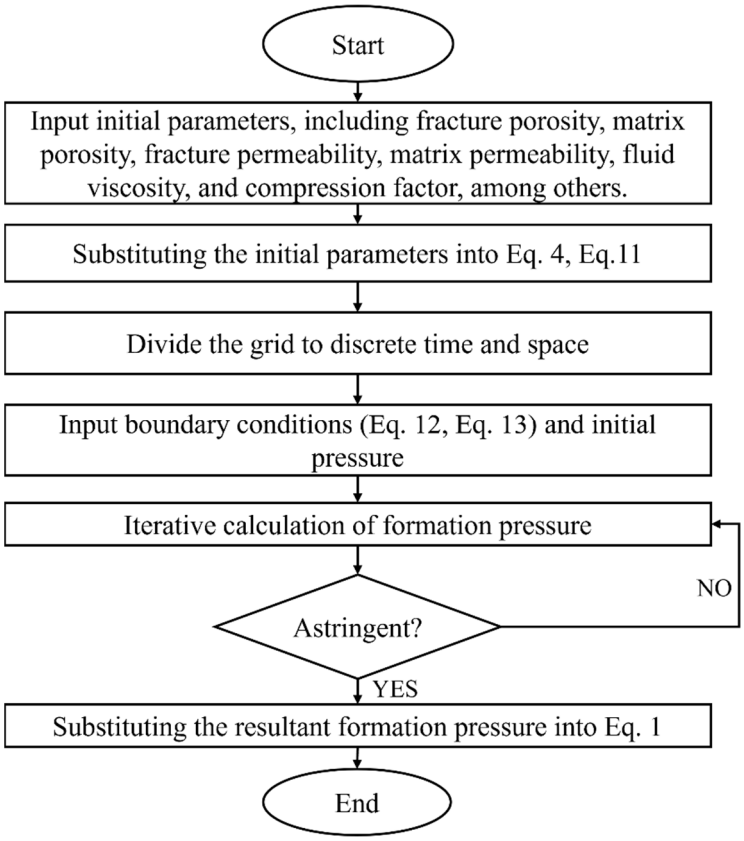

Figure 2. Flowchart for the calculation of EUR in a single well.

3. Results and Discussion

3.1. Determination of Basic Parameters

Most of China's deep shale is located in the southern Sichuan region. Therefore, based on the characteristics of tight -cutting fracturing, and referring to the geological characteristics of the southern Sichuan region and the on-site fracturing construction plan [37–40], geological basic parameters such as horizontal section length, well spacing, burial depth, reservoir thickness, and total gas content were determined. Other parameters were obtained through experimental testing, and a comprehensive reservoir control zone model for the southern Sichuan region was established. The dynamic pressure depletion process over 30 years of production was simulated using finite element analysis software [41–44], taking into account the shale gas seepage law, Knudsen diffusion, and the desorption -adsorption phenomenon. The fundamental parameters of the model are outlined in Table 1.

Table 1. Model Parameters.

Parameters	Values	Parameters	Values
Formation pressure/MPa	74	Well spacing/m	400
Geothermal temperature/°C	130	Total gas content (t/m^3)	6.25
Composition of fluid components (mol%)	methane (99%), ethane (1%)	Reservoir thickness/m	40
Average permeability of matrix/nD	120	Initial cluster spacing/m	10
Average porosity of matrix/%	4.5	Initial horizontal section length/m	1800
Fracture width/mm	5	Initial single fracture half-length/m	140
Propped fracture permeability/D	36	Buried depth/m	4000
X_e/m	2100	Y_e/m	400

When the formation temperature is 130 °C and the formation pressure is 74 MPa, the corresponding relationship between the deviation factor z and the average reservoir pressure p is calculated according to Equation (3), as shown in Figure 3. When the average reservoir pressure p is 0–15 MPa, the deviation pressure z decreases with the increase of the average reservoir pressure p. When the average reservoir pressure p is greater than 15 MPa, the deviation pressure z increases with the increase of the average reservoir pressure p. When the pressure is between 74–35 MPa, the deviation pressure z ranges from 1.03 to 1.41.

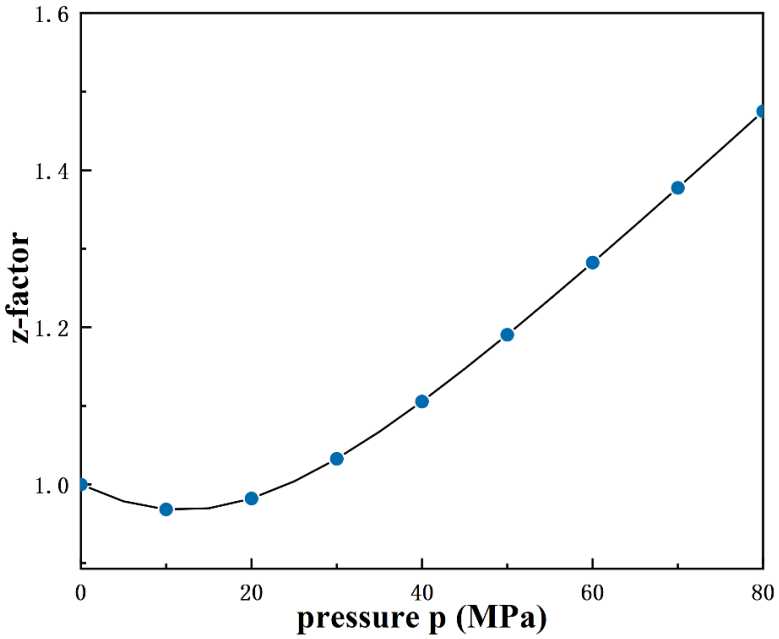

Figure 3. The relationship between the deviation factor (z) and the average reservoir pressure (p).

3.2. Fracture Half-Length Effect on EUR

The fracture half-length is varied from 100 m to 180 m, while keeping other model parameters constant, to simulate the dynamic pressure decay over 30 years of production. The simulation results are presented in Figure 4. Figure 5a illustrates the relationship between the average reservoir pressure, EUR, and production time for different fracture half-lengths. According to Formula (1), as the local layer pressure decreases, EUR increases. Notably, the variation in fracture half-length exhibits no impact on the average reservoir pressure during the initial 3 years of production. Therefore, it also does not affect the EUR. Within this period, the average growth rate of EUR is 0.156×10^8 m^3 pre year. However, after 3 years of production, the average reservoir pressure declines, and EUR increases with the growing fracture half-length over the same production time. As the fracture half-length increases, the matrix and fracture fluid flow surface expand, leading to a more rapid decline in average reservoir pressure, influencing EUR (Figure 5b). When the fracture half-length reaches 160 m, the decline in average reservoir pressure begins to stabilize, and the growth of single-well EUR slows down. Considering a simulated well distance of 400 m, the risk of interference between wells increases when the fracture half-length reaches 160 m. In conclusion, close-cut fracturing can effectively enhance single-well production, achieving a length of 0.156×10^8 m^3. Summarily, optimizing fracture half-length within the well spacing range can boost EUR, with the suitable fracture half-length range identified as 120 m~160 m under the model's simulation conditions.

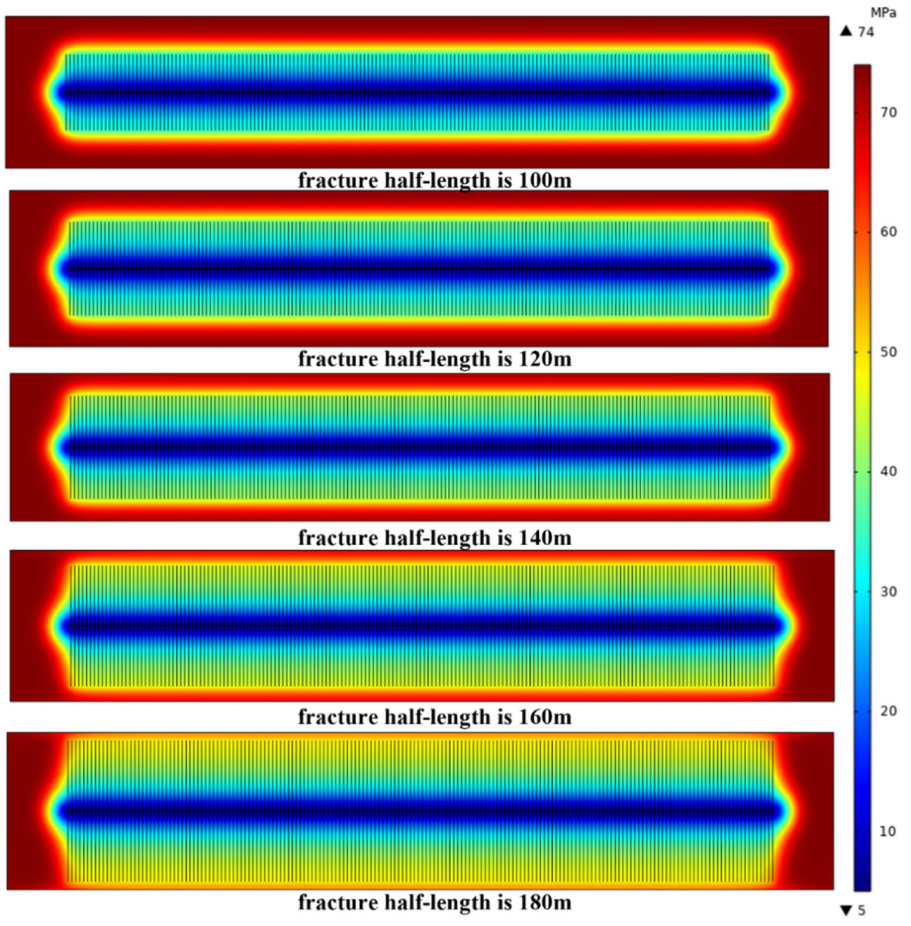

Figure 4. A cloud of simulation results over 30 years of production, varying with different fracture half-lengths.

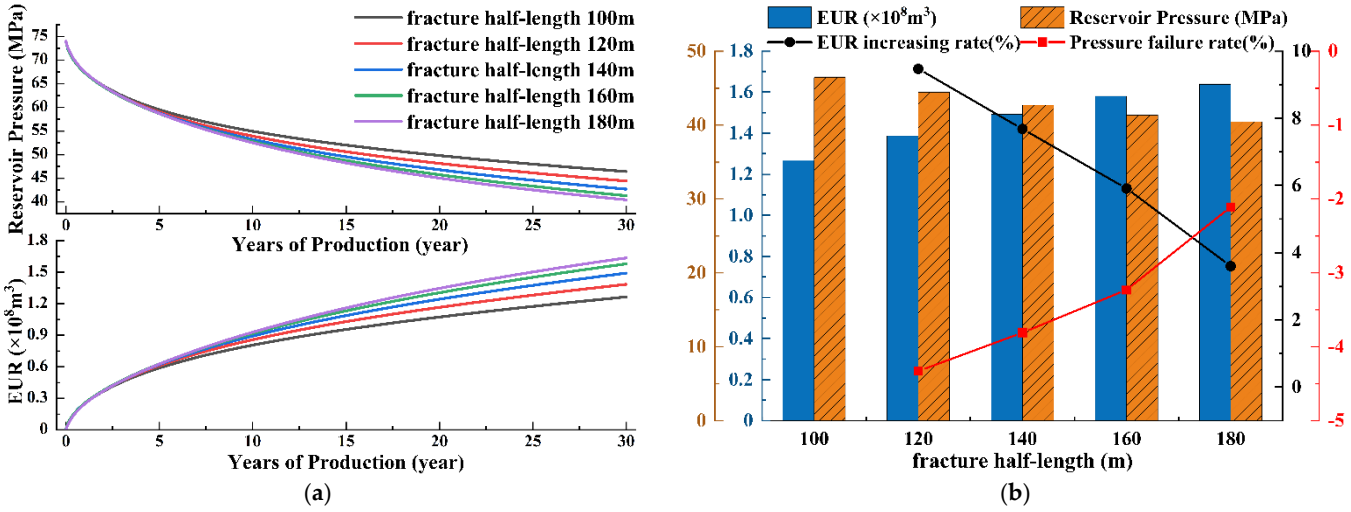

Figure 5. The impact of fracture half-length on reservoir average pressure EUR. (**a**) The relationship between fracture half-length and reservoir average pressure and EUR. (**b**) The increase rate of reservoir average pressure and EUR under different fracture half-length in 30 years of production.

3.3. Cluster Spacing Effect on EUR

The cluster spacing was systematically set at 6 m, 8 m, 10 m, 12 m, and 14 m, while maintaining constant values for other model parameters. The simulation, conducted over 30 years of production, displayed dynamic pressure decay, with results presented

in Figure 6. Figure 7a illustrates the correlation between EUR and production time for various cluster spacings, indicating an increase in EUR with the reduction of cluster spacing. Notably, the growth of EUR for cluster spacings of 10 m, 12 m, and 14 m was nearly identical in the initial 3 years of production. Specifically, during this period, the growth rates of EUR for cluster spacings of 10 m, 12 m, and 14 m were similar. Shortening the cluster spacing to 8 m led to a 17.8% increase in the average growth rate of EUR, while further shortening to 6 m resulted in a 34.6% increase. The reduction in cluster spacing enhanced shale gas desorption and adsorption, allowing more gas from the matrix to flow into the fracture, consequently increasing EUR. In Figure 7b, it is evident that the EUR growth rate for a single well rises with the decreasing cluster spacing. However, excessively small cluster spacing necessitates a more detailed fracturing scheme, increasing production costs. Therefore, a reasonable threshold for close-cut fracturing cluster spacing in actual production should be established in the field [15]. In conclusion, the cluster spacing threshold for close-cut fracturing under model simulation conditions is determined to be 8 m.

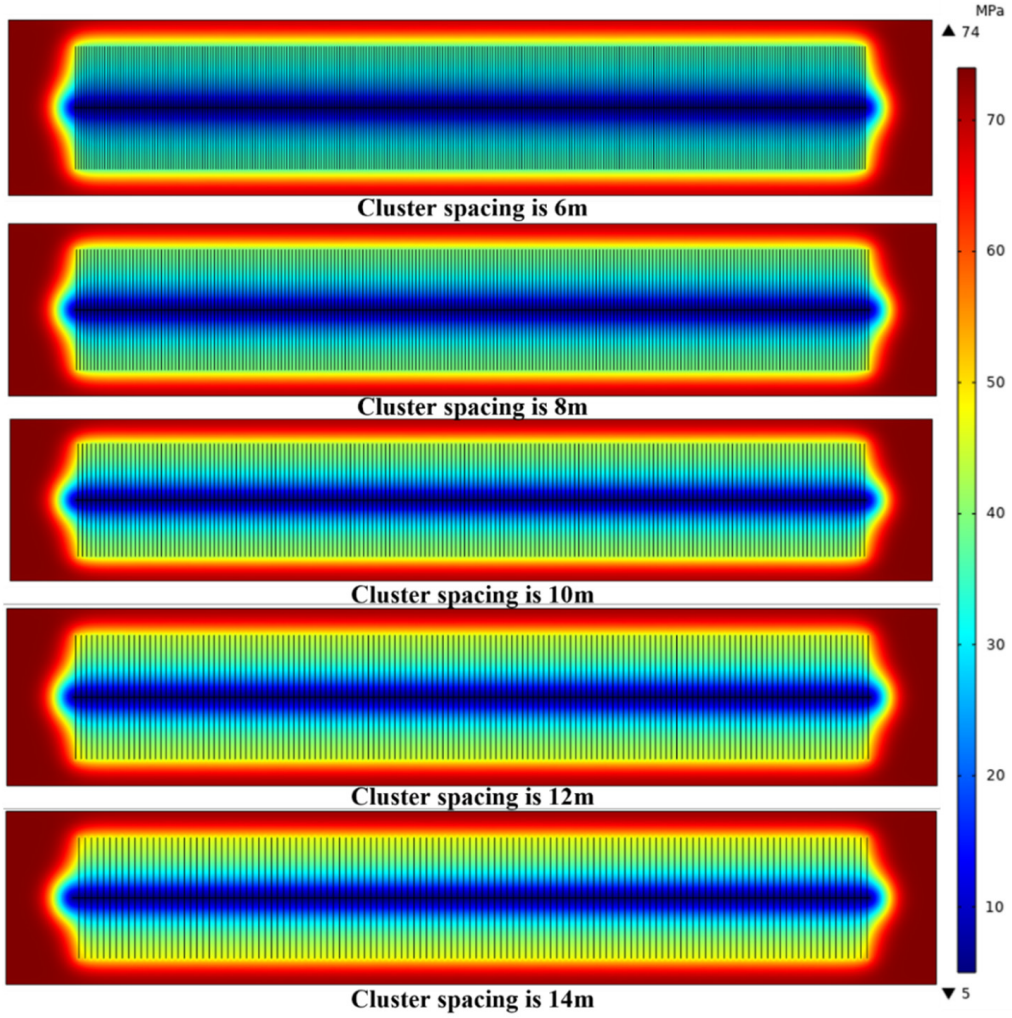

Figure 6. Modeling results of different cluster spacing production for 30 years.

3.4. Fracture Conductivity Effect on EUR

Set the fracture conductivity at 14 D·cm, 16 D·cm, 18 D·cm, 20 D·cm, and 22 D·cm while maintaining other model parameters constant. Simulate dynamic pressure failure during 30 years of production, with results presented in Figure 8. As depicted in Figure 9a, higher fracture conductivity corresponds to lower average reservoir pressure and greater EUR within the same production time. The increase in EUR is 2.8% for every 2 D·cm

increment in inflow capacity, demonstrating a proportional enhancement rate of EUR. Elevated inflow capacity accelerates seepage between the matrix and fractures, allowing more shale gas to flow from the matrix to fractures, resulting in faster reservoir pressure relief within the same timeframe and consequently increasing EUR. The EUR growth curve exhibits gradual growth as fracture conductivity increases (Figure 9b). In conclusion, when designing inflow for actual production, opt for the largest possible fracture conductivity based on real field production conditions. The optimal fracture conductivity for this model is approximately 22 D·cm.

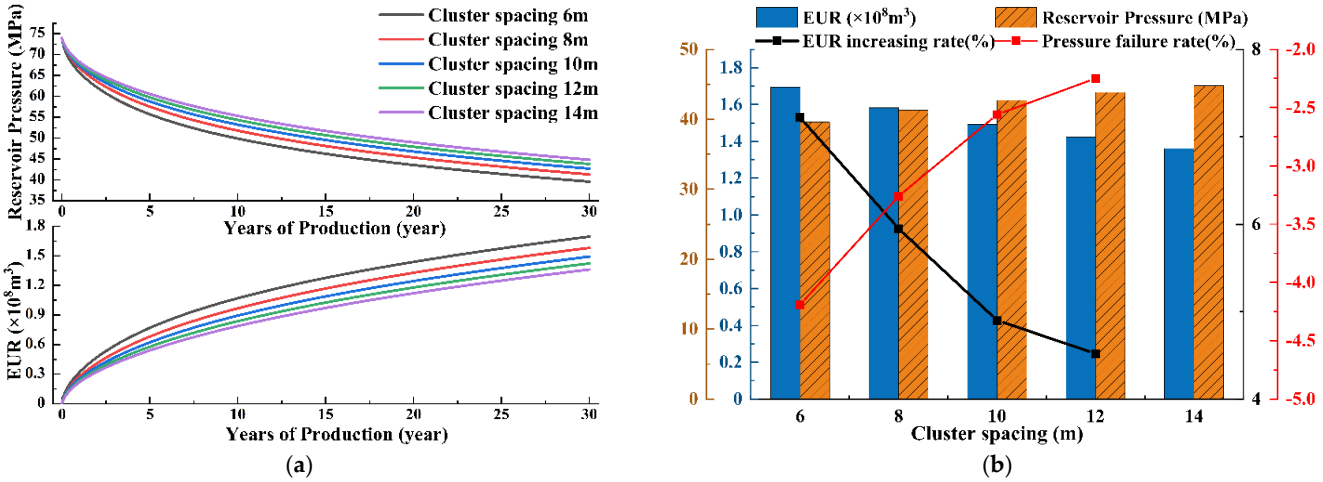

Figure 7. The impact of cluster spacing on reservoir average pressure and EUR. (**a**) The relationship between cluster spacing and reservoir average pressure and EUR. (**b**) The increase rate of reservoir average pressure and EUR under different cluster spacing in 30 years of production.

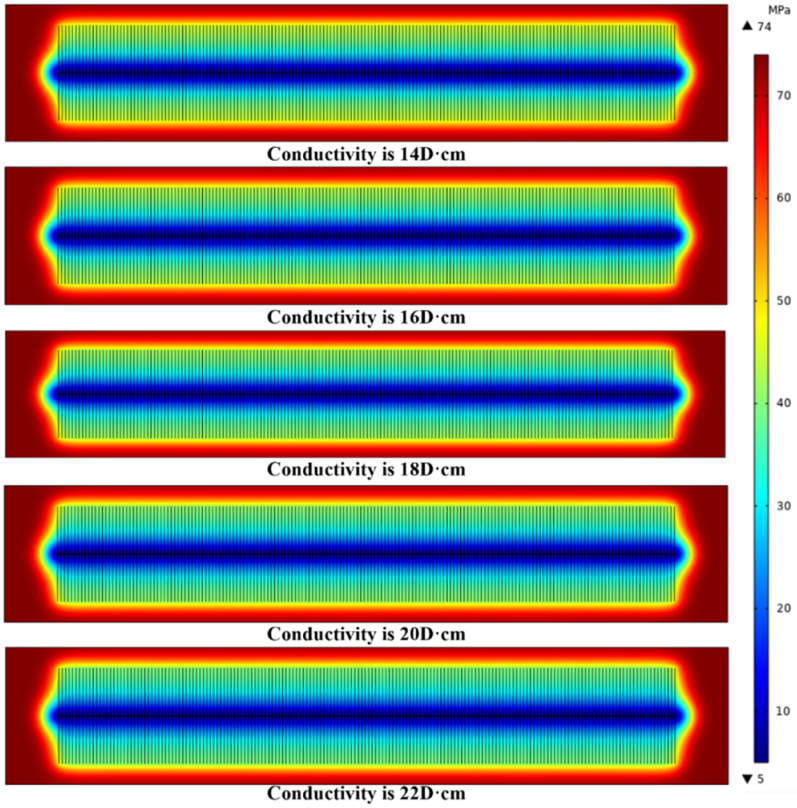

Figure 8. Modeling results of different fracture conductivity production for 30 years.

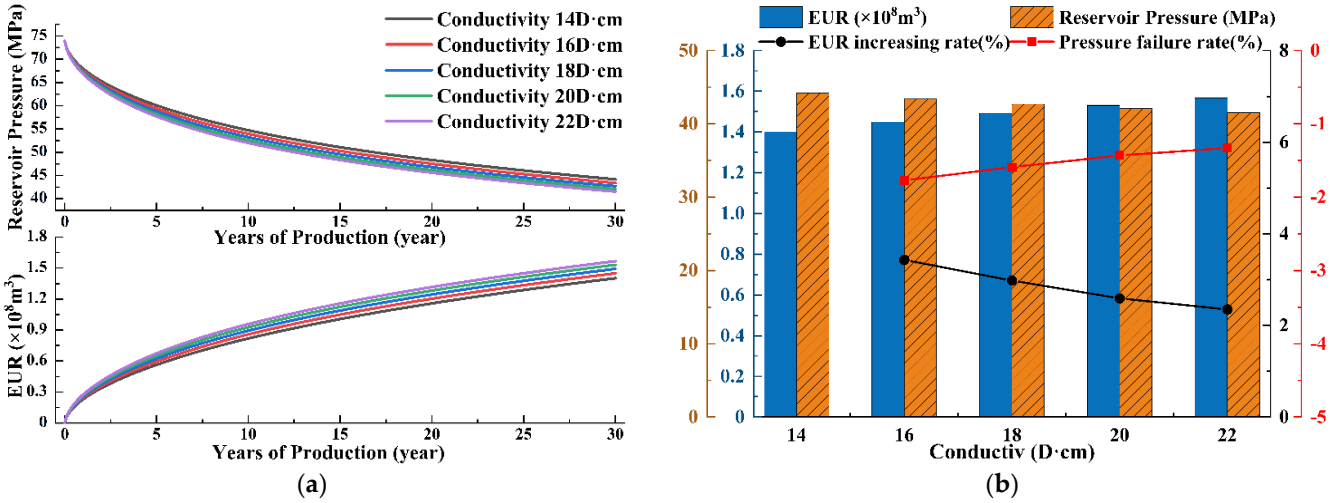

Figure 9. The impact of fracture conductivity on reservoir average pressure EUR. (**a**) The relationship between fracture conductivity and reservoir average pressure and EUR. (**b**) The increase rate of reservoir average pressure and EUR under different fracture conductivity in 30 years of production.

3.5. Horizontal Section Length Effect on EUR

Design the horizontal section length as 1400 m, 1600 m, 1800 m, 2000 m, and 2200 m while keeping other model parameters constant. Simulate the dynamic pressure failure during 30 years of production, and the results are illustrated in Figure 10. The control reserves differ for various horizontal section lengths, calculated as 4.386 × 10^8 m^3, 4.902 × 10^8 m^3, 5.418 × 10^8 m^3, 5.934 × 10^8 m^3, and 6.45 × 10^8 m^3, respectively. As depicted in Figure 11a, changes in horizontal section length have minimal impact on reservoir pressure decay, but EUR increases with longer horizontal sections. This is due to changes in total reserves. For each 200 m increase in horizontal section length, the EUR growth rate rises by 12.12% [8]. Figure 11b indicates that for the beneficial development of deep shale, the EUR of a single well should exceed 1.5 × 10^8 m^3. When the horizontal section length reaches 1800 m, the EUR reaches about 1.5 × 10^8 m^3, meeting the standard for beneficial development. In conclusion, once the cluster spacing reaches the threshold value in actual production, increasing the horizontal section length based on well area can enhance EUR. This model suggests a suitable horizontal section length exceeding 1800 m.

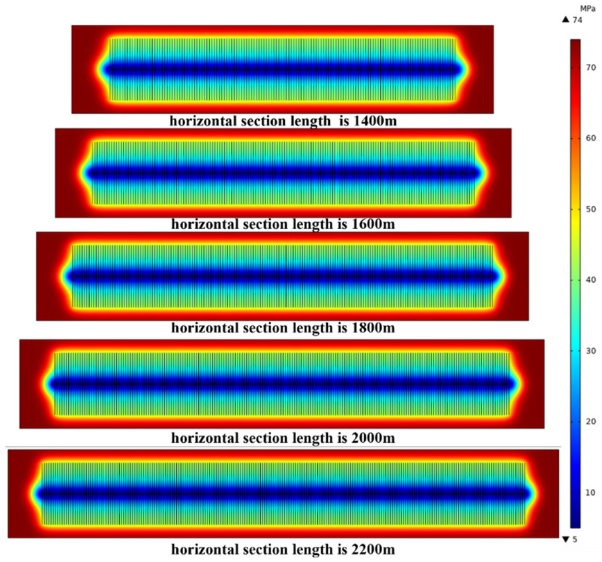

Figure 10. Modeling results of different horizontal section length production for 30 years.

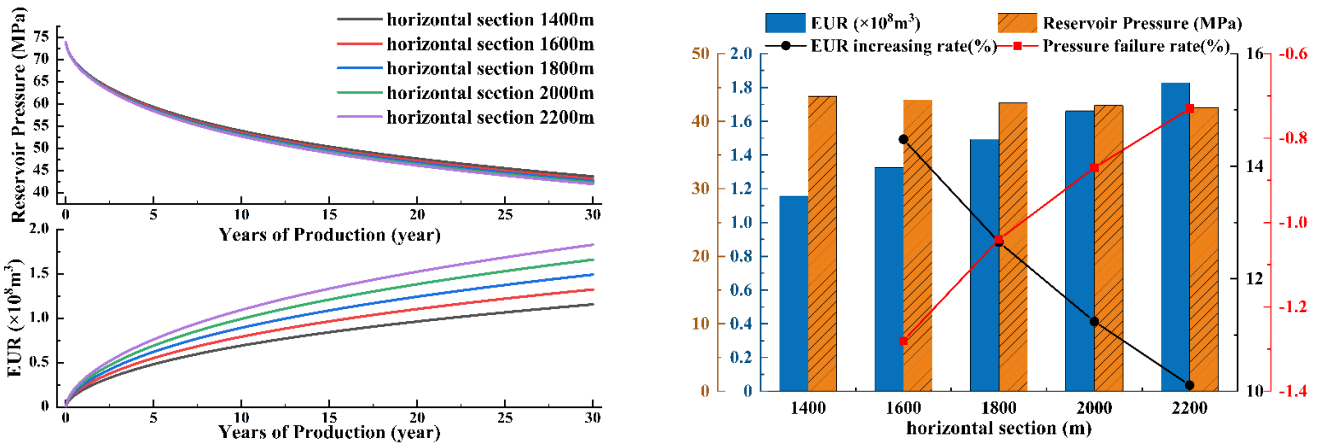

Figure 11. The impact of horizontal section length on reservoir average pressure EUR. (**a**) The relationship between horizontal section length and reservoir average pressure and EUR. (**b**) The increase rate of reservoir average pressure and EUR under different horizontal section length in 30 years of production.

3.6. Analysis of Influencing Factors

In the analysis of single-factor influence, it is evident that the magnitude of EUR is associated with fracture half-length, cluster spacing, fracture conductivity, and horizontal section length. To delve deeper into the impact of these four parameters on EUR, we employed the orthogonal experimental design method to identify the primary controlling factors influencing EUR. Subsequently, the multiple linear regression method was utilized to establish a correlation equation between the four factors and EUR.

The basic parameters and calculation results of the orthogonal experimental design are detailed in Table 2, and the analysis table of orthogonal experimental results is presented in Table 3. Synthesizing the information from Tables 2 and 3, it becomes apparent that the sensitivities of the four factors concerning EUR follow this order: horizontal section length > fracture half-length > cluster spacing > fracture conductivity.

To eliminate the impact of sample size on regression analysis, standardization was applied using the Z-score formula, as follows:

$$x_j^{(i)} = \frac{x_j^{(i)} - \frac{1}{m}\sum_{i=0}^{m-1} x_j^{(i)}}{\frac{1}{m}\sum_{i=0}^{m-1}\left(x_j^{(i)} - \frac{1}{m}\sum_{i=0}^{m-1} x_j^{(i)}\right)^2} \tag{15}$$

where m is the number of samples and n denotes the number of features.

Subsequently, the gradient descent algorithm [45] was employed to conduct linear regression analysis on the four factors influencing EUR, denoted as features x_1, x_2, x_3 and x_4. Each feature corresponds to a coefficient β, resulting in the following:

$$f(x) = \beta_1 x_1 + \beta_2 x_2 + \beta_3 x_3 + \beta_4 x_4 + C \tag{16}$$

Substituting linear equations into matrix equations as follows:

$$f_{\vec{\beta},C}(\vec{x}) = \vec{\beta} \cdot \vec{x} + C \tag{17}$$

Convergence is achieved through iterative updates of β and C, following the iterative formula below:

$$\begin{cases} J(\vec{\beta}, C) = \frac{1}{2m}\sum_{i=0}^{m-1}\left(f_{\vec{\beta},C}(\vec{x}^{(i)}) - y^{(i)}\right)^2 \\ \frac{\partial J(\vec{\beta}, C)}{\partial \beta_j} = \frac{1}{m}\sum_{i=0}^{m-1}\left(f_{\vec{\beta},C}(\vec{x}^{(i)}) - y^{(i)}\right)x_j^{(i)} \\ \frac{\partial J(\vec{\beta}, C)}{\partial C_j} = \frac{1}{m}\sum_{i=0}^{m-1}\left(f_{\vec{\beta},C}(\vec{x}^{(i)}) - y^{(i)}\right) \end{cases} \quad (18)$$

The resulting linear equation is as follows:

$$EUR = 0.1180X_1 - 0.1264X_2 + 0.2061X_3 + 0.0218X_4 + 1.4884 \quad (19)$$

where, X_1, X_2, X_3 and X_4 represent the normalized values of fracture half-length, cluster spacing, horizontal section length, and fracture conductivity, respectively.

Table 2. Orthogonal experimental design.

Number	Fracture Half-Length/m	Cluster Spacing/m	Horizontal Section Length/m	Fracture Conductivity /D·cm	EUR /$\times 10^8$ m^3
1	100	6	1400	14	1.035
2	100	8	1600	16	1.150
3	100	10	1800	18	1.266
4	100	12	2000	20	1.379
5	100	14	2200	22	1.500
6	120	6	1600	18	1.373
7	120	8	1800	20	1.490
8	120	10	2000	22	1.608
9	120	12	2200	14	1.537
10	120	14	1400	16	0.970
11	140	6	1800	22	1.773
12	140	8	2000	14	1.653
13	140	10	2200	16	1.775
14	140	12	1400	18	1.099
15	140	14	1600	20	1.242
16	160	6	2000	16	1.964
17	160	8	2200	18	2.065
18	160	10	1400	20	1.260
19	160	12	1600	22	1.404
20	160	14	1800	14	1.328
21	180	6	2200	20	2.393
22	180	8	1400	22	1.432
23	180	10	1600	14	1.347
24	180	12	1800	16	1.494
25	180	14	2000	18	1.634

Table 3. Analysis of orthogonal experimental results.

Analysis Result	Fracture Half-Length/m	Cluster Spacing/m	Horizontal Section Length/m	Fracture Conductivity /D·cm
k1	1.266	1.707	1.159	1.380
k2	1.396	1.558	1.303	1.470
k3	1.509	1.451	1.470	1.488
k4	1.604	1.383	1.647	1.553
k5	1.660	1.335	1.854	1.543
range	0.394	0.373	0.695	0.173

The correlation coefficient (R^2) of the expression is 0.962, and the relationship between the predicted and calculated values is illustrated in Figure 12.

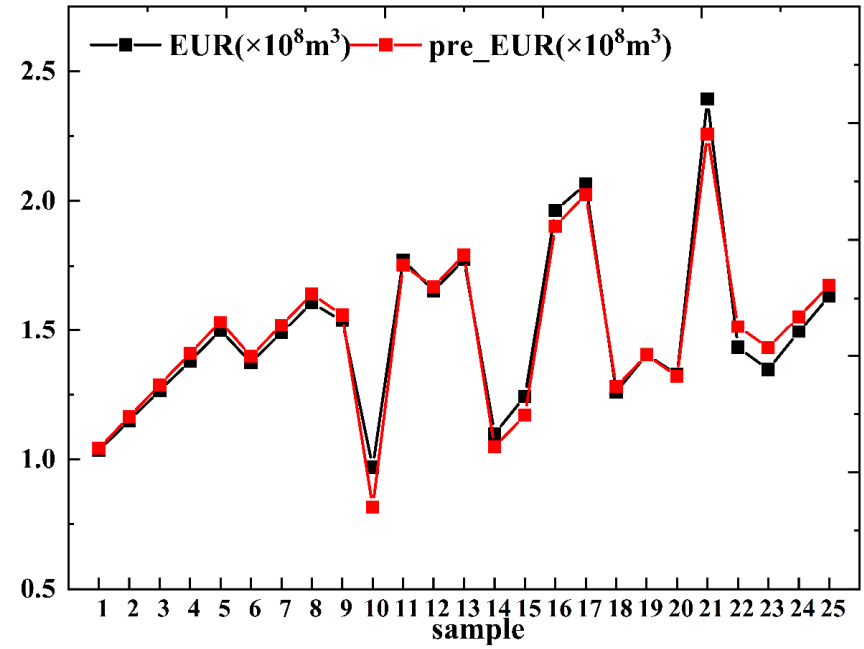

Figure 12. Relationship diagram between regression prediction and calculated value.

To validate the accuracy of linear regression, predictions were made for the test set samples. The results and analysis are presented in Figure 13.

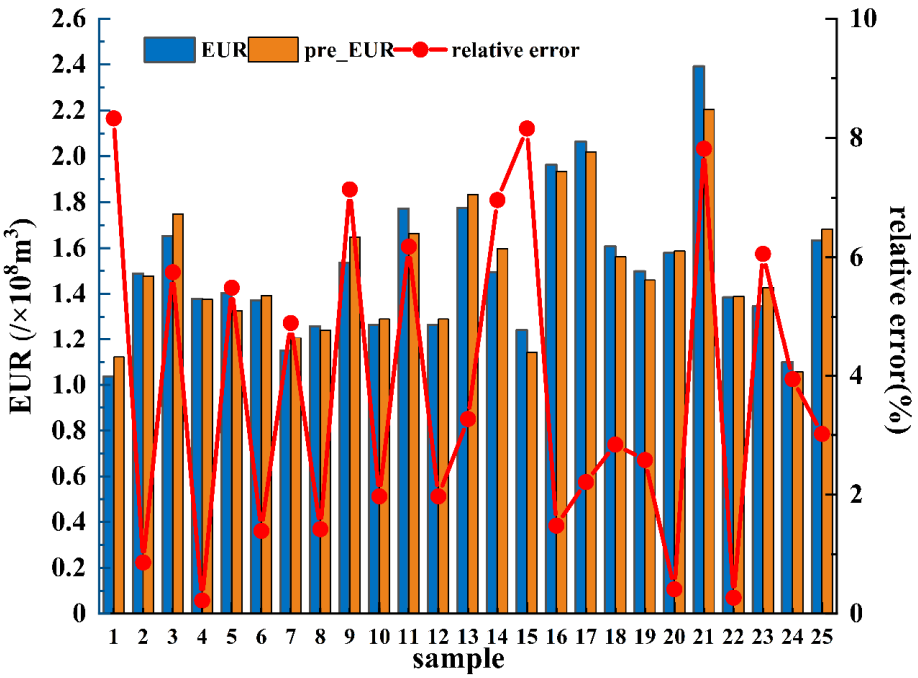

Figure 13. Test set sample prediction results and relative error analysis diagram.

The specific calculation steps are as follows: the four factors in the test set are standardized using the Equation (15), after which the standardized results are substituted as variables into the regression equation (Equation (19)) involving X_1, X_2, X_3 and X_4. Finally, the predicted EUR is obtained.

As evident from Table 4 and Figure 13, the relative errors in the predicted EUR range from 0.22% to 8.33%, with an average error of 3.79%, falling within an acceptable range. This suggests that the novel method of EUR prediction provides valuable information.

Table 4. Test set sample prediction results and relative error analysis table.

Number	Fracture Half-Length/m	Cluster Spacing/m	Horizontal Section Length/m	Fracture Conductivity /D·cm	EUR /$\times 10^8$ m^3	Pre_EUR/ $\times 10^8$ m^3	Relative Error
1	100	6	1400	14	1.035	1.121	8.33%
2	120	8	1800	20	1.490	1.477	0.85%
3	140	8	2000	14	1.653	1.748	5.75%
4	100	12	2000	20	1.379	1.376	0.22%
5	160	12	1600	22	1.404	1.327	5.49%
6	120	6	1600	18	1.373	1.392	1.39%
7	100	8	1600	16	1.150	1.206	4.90%
8	160	10	1400	20	1.260	1.242	1.42%
9	120	12	2200	14	1.537	1.647	7.14%
10	100	10	1800	18	1.266	1.291	1.97%
11	140	6	1800	22	1.773	1.663	6.18%
12	100	10	1800	18	1.266	1.291	1.97%
13	140	10	2200	16	1.775	1.833	3.27%
14	180	12	1800	16	1.494	1.598	6.96%
15	140	14	1600	20	1.242	1.141	8.16%
16	160	6	2000	16	1.964	1.934	1.49%
17	160	8	2200	18	2.065	2.019	2.21%
18	120	10	2000	22	1.608	1.562	2.84%
19	100	14	2200	22	1.500	1.461	2.58%
20	160	10	1800	18	1.581	1.587	0.41%
21	180	6	2200	20	2.393	2.206	7.82%
22	140	10	1800	18	1.386	1.390	0.27%
23	180	10	1600	14	1.347	1.428	6.06%
24	140	12	1400	18	1.099	1.056	3.94%
25	180	14	2000	18	1.634	1.683	3.02%

3.7. Model Comparison Verification

Traditional EUR prediction models include the Wattenbarger linear flow method, the PLE power-law exponential decline model, and the Duong decline model. Based on the literature [26], the Duong method is identified as the most commonly used prediction technique both domestically and internationally; thus it was selected to validate the proposed new model.

The DOUNG model solution equation is:

$$q_g(t) = q_i t^{-n} \tag{20}$$

Here, $q_g(t)$ represents the production rate at time t (10^4 m^3/d), q_i denotes the initial production rate (10^4 m^3/d), t is the production time, n is a constant, n = 0.5 (linear flow).

At a formation depth of 4000 m, the measured initial gas production is 60×10^4 m^3/d [46]. Using the Equation (20), the cumulative gas production predicted by the Duong method is calculated as 1.246×10^8 m^3. In contrast, based on the parameters in Table 1, the new method predicts a cumulative gas production of 1.386×10^8 m^3.

The results from the new prediction method differ by 14% compared to traditional approaches, primarily because traditional methods account only for shale gas seepage and adsorption-desorption effects, neglecting the Knudsen diffusion phenomenon. Con-

sequently, the new method offers greater accuracy in characterizing deep shale gas and boasts the added advantage of computational simplicity.

3.8. Discussion

This study introduces a novel perspective on the impact of close-cutting fracturing parameters on single-well EUR and its prediction. The proposed method more accurately reflects the actual conditions of shale gas reservoirs, offering simplicity and computational efficiency. However, the numerical simulation model still struggles to accurately represent the complex realities of shale gas reservoirs, indicating the need for further studies to enhance its predictive accuracy. Additionally, the numerical model exhibits certain limitations, particularly when applied to regions outside Sichuan, where significant errors may arise from variations in formation pressure and temperature. Therefore, further investigations are required to evaluate and enhance the model's broad applicability across diverse geological settings.

4. Conclusions

This study thoroughly investigates the seepage mechanisms of shale gas, including Knudsen diffusion and desorption-adsorption phenomena, providing a more realistic representation of deep shale gas behavior. The dynamic pressure depletion process of deep shale gas reservoirs is simulated using the Warren-Root model and the finite element method. The EUR of a single well post-reservoir exploitation is calculated utilizing the material balance equation for constant-volume gas reservoirs. The conclusions of this study are summarized as follows:

(1) A novel model for calculating the EUR of single wells in deep shale gas has been developed, incorporating Knudsen diffusion and adsorption-desorption phenomena while correcting apparent permeability, thereby aligning closely with the actual conditions of deep shale gas.

(2) A new EUR prediction method has been developed. Through multiple linear regression analysis of the relationships among crack half-length, cluster spacing, horizontal segment length, and fracture conductivity, a predictive expression for EUR was derived, achieving a correlation coefficient of 0.962. The average relative error between the predicted and calculated values is 3.79%, meeting accuracy requirements. Compared to tradi-tional EUR prediction approaches, this method is faster and computationally simpler.

(3) The effects of fracture half-length, cluster spacing, horizontal segment length, and fracture conductivity on the EUR of single wells under tight-cutting fracturing of deep shale were analyzed. Results indicate that fracture half-length, horizontal segment length, and fracture conductivity positively correlate with EUR, whereas cluster spacing negative-ly correlates. Orthogonal experimental analysis reveals the order of influence on EUR: hor-izontal section length > fracture half-length > cluster spacing > fracture conductivity.

(4) The new prediction methods demonstrate enhanced efficiency in estimating the range of EUR. However, their applicability remains limited. To address these shortcomings, researchers should develop robust functions or implement more optimized methodologies. Future studies will explore neural network approaches to improve prediction accuracy and better align with actual reservoir conditions.

Author Contributions: Conceptualization, T.W. and G.J.; Methodology, T.W.; Validation, T.W. and G.J.; Formal Analysis, T.W.; Investigation, T.W.; Resources, T.W.; Data Curation, T.W.; Writing—Original

Draft Preparation, T.W.; Writing—Review & Editing, T.W., G.J. and Z.X.; Project Administration, J.L. All authors have read and agreed to the published version of the manuscript.

Funding: This research received no external funding.

Data Availability Statement: Data is contained within the article. The original contributions presented in this study are included in the article. Further inquiries can be directed to the corresponding author.

Acknowledgments: The authors would like to acknowledge Ji for permission to publish this paper.

Conflicts of Interest: Author Jiansheng Liu was employed by the company Petro China Changqing Oilfield Company. The remaining authors declare that the research was conducted in the absence of any commercial or financial relationships that could be construed as a potential conflict of interest. The Petro China Changqing Oilfield Company had no role in the design of the study; in the collection, analyses, or interpretation of data; in the writing of the manuscript, or in the decision to publish the results.

References

1. Curtis, J.B. Fractured Shale-Gas Systems. *AAPG Bull.* **2002**, *86*, 1921–1938.
2. Chen, Z.; Liu, H.; Li, Y.; Shen, Z.; Xu, G. The Current Status and Development Suggestions for Shale Oil Reservoir Stimulation at Home and Abroad. *Petrol. Dril. Tech.* **2021**, *49*, 1–7.
3. Zhang, J.; Tao, J.; Li, Z.; Wang, X.; Li, X.; Jiang, S.; Wang, D.; Zhao, X. Prospect of deep shale gas resources in China. *Nat. Gas. Ind. B* **2021**, *41*, 15–28.
4. Wang, E.; Guo, T.; Li, M.; Li, C.; Dong, X.; Zhang, N.; Feng, Y. Exploration potential of different lithofacies of deep marine shale gas systems: Insight into organic matter accumulation and pore formation mechanisms. *J. Nat. Gas. Sci. Eng.* **2022**, *102*, 104563. [CrossRef]
5. He, Z.; Nie, H.; Hu, D.; Jiang, T.; Wang, R.; Zhang, Y.; Zang, G.; Lu, Z. Geological problems in the effective development of deep shale gas: A case study of Upper Ordovician Wufeng-Lower Silurian Longmaxi formations in Sichuan Basin and its periphery. *Acta Pet. Sin.* **2020**, *41*, 379–391.
6. Zou, C.; Dong, D.; Wang, Y.; Li, X.; Huang, J.; Wang, S.; Guan, Q.; Zhang, C.; Wang, H.; Liu, H.; et al. Shale gas in China: Characteristics, challenges and prospects (II). *Petrol. Explor. Deve.* **2016**, *43*, 182–196. [CrossRef]
7. Nie, H.; Li, P.; Dang, W.; Ding, J.; Sun, C.; Lie, M.; Wang, J.; Du, W.; Zhang, P.; Li, D.; et al. Enrichment characteristics and exploration directions of deep shale gas of Ordovician–Silurian in the Sichuan Basin and its surrounding areas, China. *Petrol. Explor. Deve.* **2022**, *49*, 744–757. [CrossRef]
8. Ma, X.; Wang, H.; Zhao, Q.; Liu, Y.; Zhou, S.; Hu, Z.; Xiao, Y. "Extreme utilization" development of deep shale gas in southern Sichuan Basin, SW China. *Petrol. Explor. Deve.* **2022**, *49*, 1377–1385. [CrossRef]
9. Wang, H.; Zhang, S.; Bian, X.; Li, S.; Tu, Y.; Zhang, X.; Wang, Z. Development of Fracturing Technology for Deep Shale Gas in South Sichuan, China. In Proceedings of the SPE Middle East Oil & Gas Show and Conference, Event Canceled, Sanabis, Bahrain, 28 November–1 December 2021.
10. Mindygaliyeva, B.; Uzun, O.; Amini, K.; Kazemi, H. Laboratory Measurements of Permeability and Porosity of the Matrix and Created Fractures: Application to the Pressure Falloff Analysis Following Well Stimulation to Determine Effective Fracture Spacing in Field. In Proceedings of the SPE Annual Technical Conference and Exhibition, San Antonio, TX, USA, 16–18 October 2023.
11. Wang, T.; Ye, X.; Liu, Z.; Gao, Y.; Zhuang, Z. An optimized perforation clusters spacing model based on the frictional shale layer's debonding. *Sci. China Phys. Mech. Astro* **2019**, *62*, 114621. [CrossRef]
12. Miller, C.; Waters, G.; Erik, R. Evaluation of Production Log Data from Horizontal Wells Drilled in Organic Shales. In Proceedings of the North American Unconventional Gas Conference and Exhibition, The Woodlands, TX, USA, 14–16 June 2011.
13. El Sgher, M.; Aminian, K.; Samuel, A. Impact of the Cluster Spacing on Hydraulic Fracture Conductivity and Productivity of a Marcellus Shale Horizontal Well. In Proceedings of the SPE Eastern Regional Meeting, Farmington, PA, USA, 2–3 November 2021.
14. Cheng, Y. Impacts of the Number of Perforation Clusters and Cluster Spacing on Production Performance of Horizontal Shale-Gas Wells. *SPE Res. Eval. Eng.* **2012**, *15*, 31–40. [CrossRef]
15. Cote, A.; Cameron, N.; Grunberg, D. When is There Too Much Fracture Intensity. In Proceedings of the SPE Annual Technical Conference and Exhibition, Calgary, AB, Canada, 30 September–2 October 2019.
16. O'Byrne, K.; de Groot, M.; Bonar, D.; Tkachyk, J.; Thiessen, S. A Montney Field Study Measuring the Impact of Completion Designs on near and Far Field Fracture Geometry. In Proceedings of the SPE/AAPG/SEG Unconventional Resources Technology Conference, Denver, CO, USA, 13–15 June 2023.

17. Zheng, Y.; Fan, Y.; Yong, R.; Zhaou, X. A new fracturing technology of intensive stage + high-intensity proppant injection for shale gas reservoirs. *Nat. Gas. Ind. B* **2020**, *7*, 292–297. [CrossRef]
18. Li, S.; Cai, B.; Xin, J.; Yi, X.; Li, J.; Wang, M.; Li, J.; He, C.; Zhang, H.; Yan, X.; et al. Lesson Learned from the Hydraulic Fracturing of China's Shale Oil Field. In Proceedings of the SPE/IATMI Asia Pacific Oil & Gas Conference and Exhibition, Jakarta, Indonesia, 10–12 October 2023.
19. Yang, F.; Li, B.; Wang, K.; Wen, H.; Yang, R.; Huang, Z. Extreme massive hydraulic fracturing in deep coalbed methane horizontal wells: A case study of the Linxing Block, eastern Ordos Basin, NW China. *Petrol. Explor. Develop.* **2024**, *51*, 440–452. [CrossRef]
20. Guo, J.; Lu, Q.; Liu, Z.; Zeng, F.; Guo, T.; Liu, Y.; Qui, L. Concept and key technology of "multi-scale high-density" fracturing technology: A case study of tight sandstone gas reservoirs in the western Sichuan Basin. *Nat. Gas. Ind. B.* **2023**, *10*, 283–292. [CrossRef]
21. Hu, D.; Li, Z.; Wei, Z.; Duan, J.; Miao, Z.; Pan, L.; Li, C.; Duan, H. Major advancement in oil and gas exploration of Jurassic channel sandstone in Well Bazhong 1HF in northern Sichuan Basin and its significance. *Nat. Gas. Ind. B.* **2023**, *10*, 270–282. [CrossRef]
22. Zeng, Q.; Bo, L.; Liu, L.; Li, X.; Sun, J.; Huang, Z.; Yao, J. Analysis of fracture propagation and shale gas production by intensive volume fracturing. *Appl. Math. Mech. Engl. Ed.* **2023**, *44*, 1385–1408. [CrossRef]
23. Kocon, K.; Urbancic, T.; Baig, A. Effect of Formation Stimulation Order in the Marcellus Shale. In Proceedings of the SPE/CSUR Unconventional Resources Conference—Canada, Calgary, AB, Canada, 30 September–2 October 2014.
24. Yu, S. Best Practice of Using Empirical Methods for Production Forecast and EUR Estimation in Tight/Shale Gas Reservoirs. In Proceedings of the SPE Unconventional Resources Conference Canada, Calgary, AB, Canada, 5–7 November 2013.
25. Song, H.; Su, Y.; Xiong, X.; Liu, Y.; Zhong, S.; Wang, J. EUR evaluation workflow and influence factors for shale gas well. *Nat. Gas. Geosci.* **2019**, *30*, 1531–1538.
26. Richardson, J.; Yu, W. Calculation of Estimated Ultimate Recovery and Recovery Factors of Shale-Gas Wells Using a Probabilistic Model of Original Gas in Place. *SPE Res. Eval. Eng.* **2018**, *21*, 638–653. [CrossRef]
27. Fanchi, J.R.; Cooksey, M.J.; Lehman, K.M.; Smith, A.; Fanchi, A.C.; Fanchi, C.J. Probabilistic Decline Curve Analysis of Barnett, Fayetteville, Haynesville, and Woodford Gas Shales. *J. Petrol. Sci. Eng.* **2013**, *109*, 308–311. [CrossRef]
28. Kulga, B.; Ertekin, T. Numerical representation of multi-component gas flow in stimulated shale reservoirs. *J. Nat. Gas. Sci. Eng.* **2018**, *56*, 579–592. [CrossRef]
29. Ajabshir, S.Z.; Hare, C.; Sofia, D.; Barletta, D.; Polettp, M. Investigating the effect of temperature on powder spreading behaviour in powder bed fusion additive manufacturing process by Discrete Element Method. *Powder Technol.* **2024**, *436*, 119468. [CrossRef]
30. Liang, H.; Zhang, L.; Zhao, Y.; He, X.; Wu, J.F.; Zhang, J.; Yang, J. Techno-economic and sensitivity analysis of shale gas development based on life cycle assessment. *J. Nat. Gas. Sci. Eng.* **2021**, *95*, 104183. [CrossRef]
31. Schilthuis, R.J. Active Oil and Reservoir Energy. *Trans. AIME* **1936**, *118*, 33–52. [CrossRef]
32. Dranchuk, P.M.; Abou-Kassem, H. Calculation of Z Factors For Natural Gases Using Equations of State. *J. Can. Pet. Technol.* **1975**, *14*. [CrossRef]
33. Warren, J.E.; Root, P.J. The Behavior of Naturally Fractured Reservoirs. *SPE J.* **1963**, *3*, 245–255. [CrossRef]
34. Guo, C.; Wei, M.; Chen, H.; He, X.; Bai, B. Improved Numerical Simulation for Shale Gas Reservoirs. In Proceedings of the Offshore Technology Conference-Asia, Kuala Lumpur, Malaysia, 25–28 March 2014.
35. Yang, Y.; Liu, S. Review of Shale Gas Sorption and Its Models. *Energy Fuels* **2020**, *34*, 15502–15524. [CrossRef]
36. Guo, X.; Ren, Y.; Wu, H. Shale apparent permeability model considering stress sensitivity and adsorption. *Lithol. Reserv.* **2015**, *27*, 109–112.
37. Guo, X.; Borjigin, T.; Wei, X.; Yu, L.; Lu, X.; Sun, L.; Wei, F. Occurrence mechanism and exploration potential of deep marine shale gas in Sichuan Basin. *Acta Pet. Sin.* **2022**, *43*, 453–468.
38. Jiang, T.; Bian, X.; Wang, H.; Li, S.; Jia, C.; Liu, H.; Sun, H. Volume fracturing of deep shale gas horizontal wells. *Nat. Gas. Ind. B* **2017**, *4*, 127–133. [CrossRef]
39. He, X.; Chen, G.; Wu, J.; Liu, Y.; Wu, S.; Zhang, J. Deep shale gas exploration and development in the southern Sichuan Basin: New progress and challenges. *Nat. Gas. Ind. B.* **2023**, *10*, 32–43. [CrossRef]
40. Hu, Z.; Zhao, J.; Ren, L.; Lin, R.; Hu, D.; Li, Z.; Lin, C. Exploration and Practice of Composite Temporary Plugging Fracturing Technology for Deep Shale Gas Horizontal Wells: A Case Study from X2 Well in Southeastern Sichuan. In Proceedings of the SPE Annual Technical Conference and Exhibition, San Antonio, TX, USA, 20–22 October 2023.
41. Chen, Y.; Xu, L.; Wang, L. Applications of the generic exponential production decline model on estimating well-controlled recoverable reserves of shale gas fields in the United States. *Pet. Reserv. Eval. Dev.* **2021**, *11*, 469–475.
42. Hu, Y.; Weijermars, R.; Zuo, L.; Yu, W. Benchmarking EUR estimates for hydraulically fractured wells with and without fracture hits using various DCA methods. *J. Petrol. Sci. Eng.* **2018**, *168*, 617–632. [CrossRef]
43. Wang, L.; Torres, A.; Li, X.; Fei, X.; Naido, A.; Wu, V. A Technical Review on Shale Gas Production and Unconventional Reservoirs Modeling. *Nat. Resour.* **2015**, *6*, 141–151. [CrossRef]

44. Dong, Z.; Holditch, S.A.A.; McVay, D.A.A. Resource Evaluation for Shale Gas Reservoirs. *SPE Econ. Manag.* **2013**, *5*, 5–16. [CrossRef]
45. Liu, J.; Zhao, H.; Luo, X.; Xu, J. Research progress on batch normalization of deep learning and its related algorithms. *Acta Autom. Sin.* **2020**, *46*, 1090–1120.
46. Zhang, D. Development prospect of natural gas industry in the Sichuan Basin in the next decade. *Nat. Gas. Ind. B* **2021**, *41*, 34–45. [CrossRef]

Disclaimer/Publisher's Note: The statements, opinions and data contained in all publications are solely those of the individual author(s) and contributor(s) and not of MDPI and/or the editor(s). MDPI and/or the editor(s) disclaim responsibility for any injury to people or property resulting from any ideas, methods, instructions or products referred to in the content.